INTERNATIONAL JOURNAL FOR NUMERICAL AND ANALYTICAL METHODS IN GEOMECHANICS
Int. J. Numer. Anal. Meth. Geomech., 2004; **28**:1401–1425 (DOI: 10.1002/nag.392)

K_0 estimation in level granular soil from anisotropic wave velocities on the basis of micromechanics

Y.-W. Pan[1,*,†] and J.-C. Liou[2]

[1] *Department of Civil Engineering, National Chiao-Tung University, Hsinchu 30050, Taiwan*
[2] *Energy and Resources Laboratories, Industrial Technology Research Institute, Taiwan*

SUMMARY

This study aims to explore the possibility for estimating K_0 in a level ground of granular soil by seismic methods on the basis of micromechanics theory. The idea was to simulate *in situ* cross-hole seismic method for the measurement of wave velocities along various directions of wave-propagation. This work made use of a field simulator to control a K_0 condition (zero lateral strain condition) in specimens. A series of vertical loading containing subsequent loading and unloading were applied to the specimen prepared by pluviation. In general, the K_0 values determined experimentally in this work agreed with the exiting empirical relations. K_0 value was also calibrated from measured anisotropic wave velocities using an optimization procedure. From the comparison of the back-calculated and measured results of K_0, it revealed the feasibility for the determination of the *in situ* lateral stress in granular soil by seismic methods and on the basis of micromechanics theory as long as enough wave-velocity measurements along various directions of wave-propagation were available. The potential for the usage of the presented methodology for the determination of the *in situ* lateral stress in level-ground of granular soil by seismic methods seems encouraging. Copyright © 2004 John Wiley & Sons, Ltd.

KEY WORDS: granular soil; micromechanics; K_0; wave velocities; fabric; *in situ* lateral stress

1. INTRODUCTION

In situ stress state plays an important role in many types of geotechnical problems. For instance, the frictional resistance along a pile or the lateral earth pressure acting on a retaining structure is highly dependent on the *in situ* stress state of the soil. For natural deposit in level ground, the determination of vertical stress is relatively straightforward; however, the estimation of the *in situ* horizontal stress is much more difficult.

Several empirical relations are available for the estimation of the coefficient of lateral earth pressure K_0, which is the ratio between the lateral horizontal stress and the vertical stress in at rest condition. For normally consolidated clay or initially loaded sand, K_0 and the frictional

*Correspondence to: Y. -W. Pan, Department of Civil Engineering, National Chiao-Tung University, 1001 Ta-Hsueh Road, Hsinchu 30050, Taiwan.
† E-mail: ywpan@mail.nctu.edu.tw

Contract/grant sponsor: National Science Council of the Republic of China; contract/grant number: NSC90-2211-E-009-068

Received 26 February 2004
Revised 28 May 2004

angle ϕ' appear to have good correlation in a form such as that suggested by the Jaky's equation [1]. The stress history also affects the lateral earth pressure of a soil. For overconsolidated clay or unloaded sand, K_0 depends on the overconsolidation ratio (OCR) [2].

Several approaches were developed to determine the *in situ* lateral stress. Among them include spade-shaped total earth pressure cell [3], flat dilatometer [4], and pressuremeter test [5–7]. Soil disturbance appears to be a common problem for those methods because that the local stress may be affected by disturbance or stress release due to the process of equipment push-in or installation or drilling. Among various approaches, the self-boring pressuremeter was designed to minimize the influence of soil disturbance. On the other hand, total earth pressure cell is capable of detecting a change in local stress. Nevertheless, any approach that can avoid soil disturbance and can somehow take into account the average stress in a relatively large domain adjacent to the test position should be superior and desirable.

Seismic methods such as the down-hole or cross-hole method have been well established and accepted in geotechnical practice [8–11]. Wave velocities are the major products of the seismic methods; the wave velocities of a geo-material depend primarily on the material's elastic stiffness. Traditionally, wave velocities determined by these methods are used to characterize the elastic properties or to estimate the substrata profile.

For a granular material such as sand, the elastic stiffness is a function of its fabric and stress state. While the wave velocities for an unstrained granular material depend on its elastic stiffness, it is reasonable to infer that the wave velocity of a granular assembly is also a function of its fabric and stress state. Using a relationship between shear velocity and stress state [12], Sully and Campanella [13] and Fioravante *et al*. [14] estimated K_0 from measured anisotropic shear velocities. They assumed that soil is a transversely isotropic material and the principal stresses are on the vertical and the horizontal planes. Sully and Campanella [13] concluded that the shear velocity ratio (the ratio of horizontal and vertical wave velocities) depends on the structural anisotropy and the stress state of soil, while the influence of structure anisotropy is stronger than that of stress state. Consequently, it appears any attempt to closely estimate K_0 from measured shear velocities should try to identify soil fabric simultaneously and correctly.

If sufficient measurements of wave velocities can be obtained along various directions of wave-propagation, it should be possible to deduce both fabric and K_0 from a set of measured wave-velocities for level ground. The present work attempts to explore the possibility for the estimation of *in situ* lateral stress using seismic method. In this work, large sand specimens were placed in a calibration chamber with accurate control over the applied stress states in subsequent loading/unloading stages. At each loading stage, wave velocities along various directions were measured using miniature geophones placed inside the specimen. The measured anisotropic wave velocities were then used to estimate K_0. The following context includes, in order, the theoretical background of the proposed methodology, the experimental set-up, the results and discussions, and the conclusions of this study.

2. THEORETICAL BACKGROUND

The proposed approach for the estimation of K_0 from measured anisotropic wave velocities involves an analytical procedure similar to the one proposed by Pan and Dong [15] for evaluating the fabric of a granular assembly. It contains three basic elements: (i) a stress-dependent micromechanics-based elastic model; (ii) a theory of elastic wave propagation for

anisotropic material; and (iii) an optimization method. Figure 1 outlines the conceptual procedure. This section presents a brief review of this approach.

2.1. Stress-dependent micromechanics-based elastic model

The fabric of a granular material determines the mechanical behaviour of the material. Fabric of a granular assembly can be categorized into geometric fabric (characteristics of microstructure) and kinetic fabric (contact-force distribution). With prescribed fabric conditions, the elastic constitutive relations can be determined on the basis of micromechanics. For example, Chang and Misra [16] derived the elastic stiffness C_{ijkl} of an idealized granular assembly (a granular assembly composed of equal-sized spherical particles) containing M contacts in a representative volume V as follows.

$$C_{ijkl} = \frac{1}{V}\sum_{c}^{M} \ell_i^c k_{jl}^c \ell_k^c = \frac{M}{V}\int_{\Omega} 4r^2 n_i k_{jl}^c n_k E(\mathbf{n})\,\mathrm{d}\Omega \tag{1}$$

in which $\ell_i^c = \ell \cdot \mathbf{n}_i^{\tilde{\ell}} = 2 \cdot r \cdot \mathbf{n}_i^c$ is the branch-vector connecting two adjacent particles' centroids in the cth contact point; r is the radius of the spherical particles; ℓ is the branch-vector-length; and $\mathbf{n}_i^{\tilde{\ell}}$ is the unit branch-vector, identical with the contact normal $\mathbf{n}_i^c$ for an idealized granular assembly. The term $k_{jl}^c = k_n^c \cdot n_j^c \cdot n_l^c + k_s^c \cdot s_j^c \cdot s_l^c + k_t^c \cdot t_j^c \cdot t_l^c$ is the local contact stiffness. The terms k_n^c, k_s^c and k_t^c, respectively, are the contact stiffness along the directions of **n**, **s** and **t**, which are the three base vectors of the local co-ordinate system shown in Figure 2. The direction-dependent function $E(\mathbf{n})$ stands for the density function of the contact normal in the **n** direction. The integration $\int_{\Omega}(\cdot)\cdot E(\mathbf{n})\,\mathrm{d}\Omega$ stands for the double integration $\int_0^{\pi}\int_0^{2\pi}(\cdot)\cdot E(\omega,\psi)\cdot \mathbf{sin}\,\theta\,\mathrm{d}\omega\,\mathrm{d}\psi$, where ω and ψ (with the ranges of $0 \leqslant \omega \leqslant 2\pi$ and $0 \leqslant \psi \leqslant \pi$, respectively) are defined in Figure 2; $\mathrm{d}\Omega = \mathbf{sin}\,\theta\,\mathrm{d}\omega\,\mathrm{d}\psi$ is the elementary solid angle in a spherical co-ordinate system. Pan and Dong [15] derived a generalized form of Equation (1) for a granular assembly composed of graded spherical particles to allow for the consideration of grain-size distribution. They also demonstrated that the initial stiffness is independent of grain size and uniformity as long as its void ratio and average co-ordination number remain unchanged.

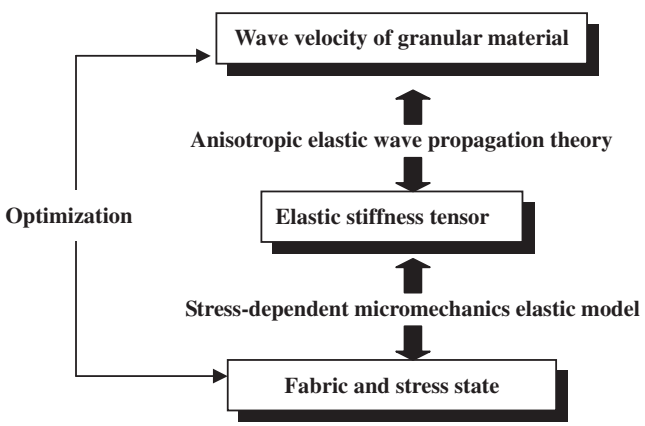

Figure 1. Analytical procedure for determining fabric and stress state of a granular material from measured wave velocity (modify from Reference [15]).

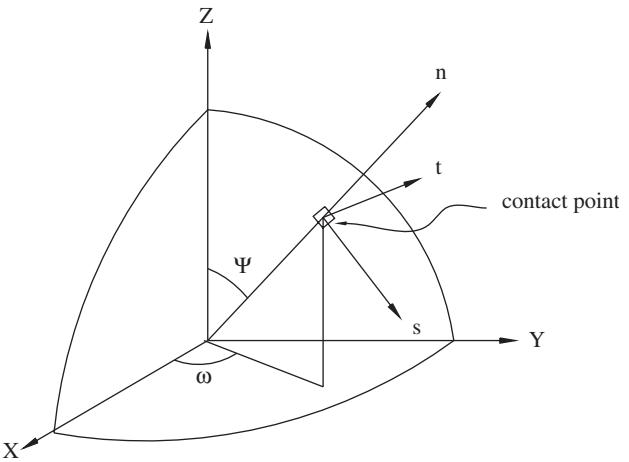

Figure 2. Spherical co-ordinate system.

Based on the Hertz–Mindlin contact theory, the averaged local normal contact stiffness $\bar{k}_n(\mathbf{n})$ and shear contact stiffness $\bar{k}_r(\mathbf{n})$ of the grouped contact points in the **n** direction can be expressed as functions of contact forces. The averaged local normal contact stiffness $\bar{k}_n(\mathbf{n})$ is related to averaged normal contact force $\bar{f}_n(\mathbf{n})$ as follows.

$$\bar{k}_n(\mathbf{n}) = C_1 \cdot (\bar{f}_n(\mathbf{n}))^{1-2\alpha} \tag{2}$$

The coefficient C_1 is dependent of the radius of contact surface and the elastic constants of particle solid; α is a material parameter. According to the Hertz–Mindlin contact theory, $\alpha = 1/3$ and $C_1 = (\frac{1}{2\alpha}) \cdot (\frac{16}{9})^{\alpha} \cdot (\bar{R})^{\alpha} \cdot (G_s/(1-\upsilon_s))^{2\alpha}$, in which G_s and υ_s are the shear modulus and the Poisson's ratio, respectively, of particle solid. The averaged shear contact stiffness $\bar{k}_r(\mathbf{n})$ can also be related to contact forces as follows.

$$\bar{k}_r(\mathbf{n}) = C_2 \cdot \left(1 - \frac{\bar{f}_r(\mathbf{n})}{\bar{f}_n(\mathbf{n}) \cdot \tan \phi_\mu}\right)^{\beta} \cdot k_n = \lambda \cdot \bar{k}_n(\mathbf{n}) \tag{3}$$

In the above equation, $\bar{f}_r(\mathbf{n})$ is the averaged shear contact force; C_2 is a coefficient dependent of the Poisson's ratio of particle solid; ϕ_μ is the inter-particle frictional angle; λ is the stiffness ratio; and β is a material parameter. According to the Hertz–Mindlin contact theory, $C_2 = (2(1-\upsilon_s))/(2-\upsilon_s)$ and $\beta = 1/3$; $\bar{R}$ is the relative radius of curvature of contact surfaces; for an idealized assembly of spheres with radius r, $\bar{R} = r/2$.

Fabric involved in the above equations is directional variable, and can be described in tensor forms [17], or in a Fourier series [18], or in a spherical harmonics expansion [16]. Kanatani [17] proposes a polynomial expansion in terms of vector **n** to represent the density function of a fabric variable. He defined several kinds of fabric tensors. Among various forms of fabric tensors, the third kind fabric tensor can be described as follows.

$$E(\mathbf{n}) = (1 + D_{ij} n_i n_j + D_{ijkl} n_i n_j n_k n_l + \cdots + D_{i_1 \cdots i_n} n_{i_1} \cdots n_{i_n} + \cdots)/4\pi \tag{4}$$

in which the tensor $D_{i_1 \cdots i_n}$ is called the 'fabric tensor of the third kind' of rank n. Liou and Pan [19] derived the correlations between the coefficients of fabric tensor up to rank 4 for a

transversely isotropic granular assembly and used those correlations to evaluate the geometric fabric of the assembly on the basis of micromechanics.

The contact-force distribution (i.e. kinetic fabric) has to be determined in order to evaluate $\bar{k}_n(\mathbf{n})$ and $\bar{k}_r(\mathbf{n})$. For an idealized granular assembly, the averaged contact-force can be estimated from the stress tensor σ_{ij} and packing structure using the static hypothesis of Chang *et al.* [20] as

$$\bar{f}_j^c = \sigma_{ij} \cdot A_{ik} \cdot n_k^c \tag{5}$$

in which $\bar{f}_j^c$ is the contact-force at the cth contact point of the granular assembly containing M contacts in a representative volume V. In the above equation, A_{ik} is a tensor relating to the contact-normal distribution of the granular assembly; the tensor A_{ik} satisfies $A_{ik} \cdot F_{kq} = \delta_{iq}$ where $F_{ik} = (A_{ik})^{-1} = (2 \cdot r \cdot M/V) \cdot N_{ik}$; N_{ik} is the fabric tensor of the first kind representing the sample mean of contact-normal distribution for which $N_{ik} = \frac{2}{15} \cdot D_{ik} + \frac{1}{3} \cdot \delta_{ik}$. Once both the stress-state and the geometric fabric are determined, the contact force can be evaluated.

2.2. Theory of elastic wave propagation for transversely isotropic material

Natural granular deposits are often transversely isotropic. Using the Voigt's notation, the stress and strain tensors, respectively, can be expressed as $\sigma_m = [\sigma_{11},\ \sigma_{22},\ \sigma_{33},\ \tau_{12},\ \tau_{13},\ \tau_{23}]^{\mathrm{T}}$ and $\varepsilon_n = [\varepsilon_{11},\ \varepsilon_{22},\ \varepsilon_{33},\ \gamma_{12},\ \gamma_{13},\ \gamma_{23}]^{\mathrm{T}}$, in which m, n are the index 1–6. The global constitutive law can be expressed as $\sigma_m = E_{mn} \cdot \varepsilon_n$, the components have to satisfy $E_{mn} = E_{nm}$ due to symmetry. For a transversely isotropic granular material with the axis-3 as the rotation-symmetry axis, the number of independent elastic constants reduces to five (i.e. E_{11}, E_{33}, E_{12}, E_{13} and E_{66}). Other elastic constants are $E_{22} = E_{11}$, $E_{23} = E_{13}$, $E_{55} = E_{66}$, $E_{44} = (E_{11} - E_{12})/2$ and the rest are equal to 0. Relation exists between the elastic stiffness tensor and the wave velocity of a transversely isotropic elastic material [21]. The elastic wave-velocity of a transversely isotropic material depends on the inclined angle θ between the rotation-symmetry axis and the wave-propagation direction. One primary wave velocity $V_{p\text{-}\theta}$ and two shear-wave velocities $V_{sh\text{-}\theta}, V_{sv\text{-}\theta}$ in the direction inclined at an angle θ with the rotation-symmetry axis can be formulated as follows [15]. Figure 3 illustrates the schematic definitions of $V_{sh\text{-}\theta}$ and $V_{sv\text{-}\theta}$.

$$V_{sh\text{-}\theta} = \sqrt{(E_{66} \cdot \cos^2\theta + E_{44} \cdot \sin^2\theta)/\rho_d} \tag{6}$$

$$V_{p\text{-}\theta} = \sqrt{(-b + \sqrt{b^2 - 4 \cdot c})/2\rho_d} \tag{7}$$

$$V_{sv\text{-}\theta} = \sqrt{(-b - \sqrt{b^2 - 4 \cdot c})/2\rho_d} \tag{8}$$

in which ρ_d is the mass density and

$$b = -(E_{11} \sin^2\theta + E_{33} \cos^2\theta + E_{66}) \tag{9}$$

$$c = (E_{11} \sin^2\theta + E_{66} \cos^2\theta) \cdot (E_{66} \sin^2\theta + E_{33} \cos^2\theta) - (E_{13} + E_{66})^2 \cos^2\theta \sin^2\theta \tag{10}$$

In the remaining section, an assembly of granular materials is assumed transversely isotropic.

2.3. Optimization method

The wave velocities for soil depend on elastic stiffness. Also, the elastic stiffness is a function of fabric and stress state of a granular assembly. Consequently, the wave velocity of granular

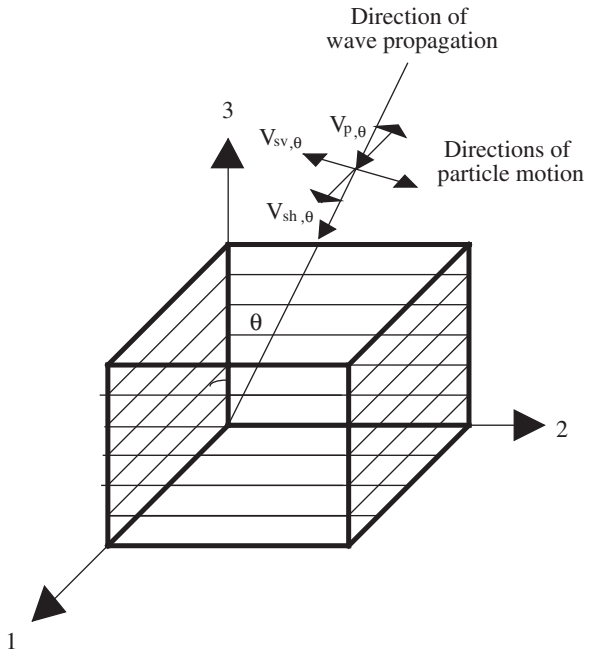

Figure 3. Directions of primary and shear wave propagation and polarization through a transversely isotropic material [15].

material should also be a function of fabric and stress state. If sufficient number of measurement of wave velocities can be obtained along different directions of wave propagation, it should be possible to obtain fabric and stress state from a set of measured wave velocities employing back calculation by optimization. Since the vertical stress in level ground can be determined directly, the unknowns, in general, are K_0 as well as fabric.

An optimization aims to search for the optimized value of a non-linear object function $\Phi\{x\}$. A combination of the genetic algorithm [22] and nonlinear optimization by the Levenberg–Marquardt method [23] were incorporated to search for the most suitable stress state from a set of measured wave velocities.

The object function $\Phi\{x\}$ in this case is defined as the average of normalized differences between 'n' (model) calculated data, $U_i(\{x\}),\ (i = 1, n)$ and 'n' measured data of wave-velocity, $V_i,\ (i = 1, n)$ as follows:

$$\Phi\{x\} = \sqrt{\frac{\sum_{i=1}^{n} [(U_i(\{x\}) - V_i)/U_i(\{x\})]^2}{n}} \tag{11}$$

in which $\{x\}$ is the vector containing the unknown parameters. In the present work, $E(\mathbf{n})$ is approximated by a fabric tensor of rank 2, i.e. $E(\mathbf{n}) = (1 + D_{ij}n_in_j)/4\pi$; thus the unknown parameters $\{x\}$ includes only α, β, D_{33} and K_0. The involved non-linear optimization, then, aims to search for a set of unknown parameters $\{x\}$ corresponding to a series of $U_i(\{x\}),\ (i = 1, n)$ such that the object function becomes minimum.

The procedure of optimization began with the genetic algorithm to obtain a number of solutions as the candidates. These candidates then were input as the initial guess of solution in the nonlinear optimization by the Levenberg–Marquardt method in order to refine the solution. This combined use of optimization worked pretty well.

3. EXPERIMENTAL SET-UP AND PROCEDURE

3.1. Experimental set-up

The sample used in the tests was Ottawa Sand (C-778) with the index properties listed in Table I. The Ottawa sand contains roughly round shaped particles. The equipment set-up that housed the test specimen and controlled the stress condition was an axis-symmetric field simulator [24], originally designed to serve as a calibration chamber for cone penetration tests. The simulator is a close-loop control system that is capable of controlling the boundary condition of the lateral stress/strain. The sand specimen, 784 mm in diameter and up to 910 mm in height, is housed in a stack of up to eleven rings made of steel; each ring (80.5 mm high) is lined with an inflatable silicone rubber membrane on the inside to allow circumferential displacement (extensometer) measurement and stress control (by air pressure). To minimize frictional forces between sand and rubber membranes, the whole ring stack is supported on four air bellows [24]. The ring stack altogether is allowed to move downward when the specimen is loaded. This arrangement is similar to a floating ring design in an oedometer. Specimens were prepared by dry pluviation using a sand-rainer. The relative density of the specimen was roughly controlled by the opening slot size of the sand-rainer's base. Figure 4 shows the layout of the field simulator. Detail about the apparatus should refer to Hsu and Huang [24].

The equipments for measuring the wave velocities included a wave generator (HP 33120A), an amplifier, and a series of miniature geophones (served as either the wave activators or the receivers). Figure 5 shows the layout of test equipments. The geophones used were G*S*-100, made by GeoSpace, 31.8 mm in diameter, 35 mm high, with a natural frequency of 100 Hz. A spectrum analyser, called 'Signal Doctor Spectrum Analysis System', made by Prowave Engineering, was employed for the acquisition and analysis of wave signals. This spectrum analyser can handle wave signals with frequency below 20 kHz.

The wave velocity was determined by dividing the distance between the wave activator and receiver by the travel time. Figure 6 shows the layout of geophones. Twenty-two geophones were installed in five subsequent layers. The geophones in the 3rd layer were arranged to

Table I. Properties of Ottawa Sand (C-778).

Mineral	Quartz
Shape	Rounded
e_{max}	0.76
e_{min}	0.50
G_s	2.65
D_{60} (mm)	0.36
D_{10} (mm)	0.23
C_u	1.56

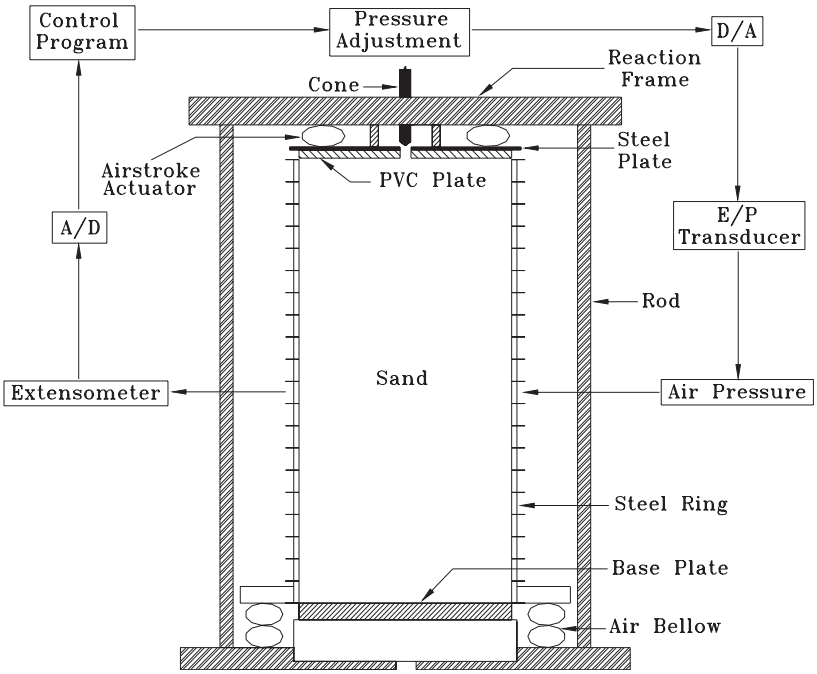

Figure 4. Layout of field simulator [24].

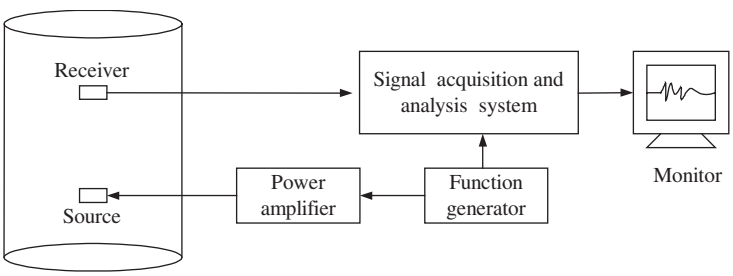

Figure 5. Layout of equipments.

measure the wave-velocity propagating along the horizontal direction (e.g. 5-5′ for $V_{p\text{-}90}$, 9-9′ for $V_{sh\text{-}90}$, and 11-11′ for $V_{sv\text{-}90}$). The geophones in other layers were arranged to measure the wave-velocity propagating along either the vertical or an oblique direction. Those geophones lain on the 1st and 5th layers were in pairs: 1-1′ and 6-6′ for $V_{p\text{-}0}$; 2-2′ and 3-3′ for $V_{p\text{-}\theta}$ along various θ; 7-7′ for $V_{sh\text{-}0}$; 8-8′ and 10-10′, respectively, for V_{sh} and V_{sv} along an oblique direction. A pair of geophones, labeled as '4' and '4′', lain on the 4th and 2nd layers, respectively, were arranged to measure V_p along a larger oblique angle θ.

Each geophone was served as either a triggering source or a receiver. The distance between each pair of geophones (between the source and the receiver) was generally within 0.4 and 0.6 m. A wave generator produced a sinusoidal wave at each source geophone in turn. The peak-to-peak voltage of the sinusoidal wave was maintained at 10 V. To minimize the near-field effects,

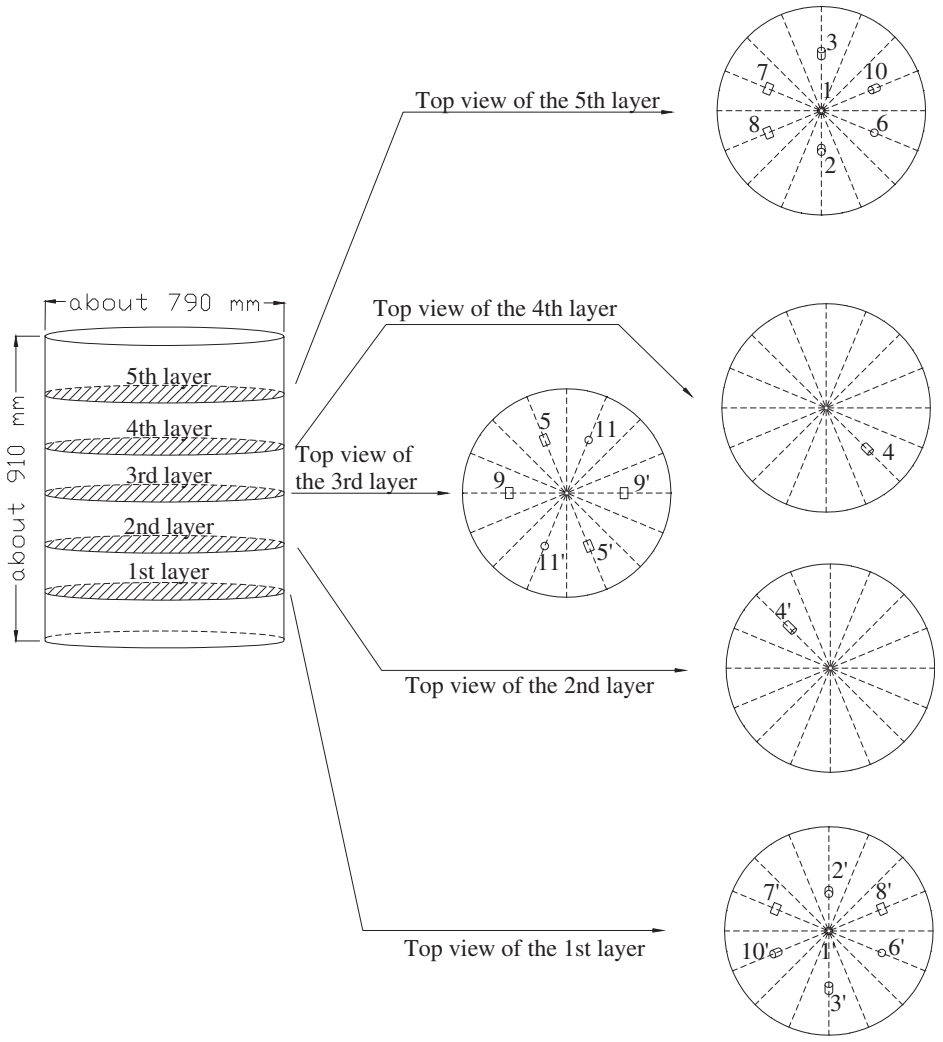

Figure 6. Layout of geophones in a specimen.

the triggered frequency of wave signal was 1500 Hz for *S*-wave and 2000 Hz for *P*-wave in order to satisfy two criteria: (1) the wave length was greater than three times the size of geophones, and (2) the wave length was smaller than one half of the distance between the source and receiver (i.e. the travel distance) geophones [25]. In the experiments, the distance between any source and receiver was kept at least one and half times of wavelength to reduce the near field effect while ensuring a recognizable wave signal can be picked up.

3.2. Experimental procedure

The pluviation for preparing the specimen proceeded in six stages. As the specimen reached a specific elevation, the pluviation was halted and the geophones were installed. The top plate was

placed after the completion of the full specimen. The center of the sand-rainer's base must aim at the center of the chamber to ensure specimen's homogeneity, and the pluviation must be carried out with care.

During the whole course of a test (including the air-pluviated preparation of specimen and the application of loading), the lateral boundary of specimen was maintained at a near K_0 condition (zero lateral strain condition) . During pluviation, the lateral stress in each ring was adjusted individually to allow the circumferential deformation within ± 0.01 mm (corresponding to a strain within $\pm 4 \times 10^{-6}$). The threshold deformation was able to simulate K_0 condition and exempt from the influence of signal noise. During loading application, the lateral stresses were adjusted according to the average circumferential deformation of a couple of intermediate rings; the average circumferential displacement was maintained within ± 0.005 mm (corresponding to a lateral strain within $\pm 2 \times 10^{-6}$). The same incremental lateral stress was applied to all rings simultaneously.

The vertical loading was applied in a sequence of 0 kPa $\rightarrow$ 26.73 kPa $\rightarrow$ 51.7 kPa $\rightarrow$ 100.05 kPa $\rightarrow$ 51.7 kPa $\rightarrow$ 26.73 kPa $\rightarrow$ 0 kPa while the specimen was maintained in K_0 condition. In addition to the applied loading, the specimen was subjected to an initial stress from its self-weight and the weight of top plate. The initial vertical stress due to its self-weight was 7.2 kPa (for $D_r = 62.3\%$) or 7.61 kPa (for $D_r = 95\%$) at specimen's mid-height; the top-plate's weight resulted in additional 3.47 kPa. They made a total of 10.67 kPa (for $D_r = 62.3\%$) or 11.08 kPa (for $D_r = 95\%$). For each loading stage, the P- and S-wave velocities between each pair of the source and receiver geophones were measured to obtain wave velocities along various directions of wave-propagation. The size of the field simulator inevitably limited the maximum number of installed geophones. For each test stage, a total of ten wave velocities were measured, including five P-wave velocities, three S_h-wave velocities, and two S_v-wave velocities along various directions of wave-propagation. The loading/unloading rate was about 1 kPa/min, slowly enough to avoid any dynamic effect.

4. RESULTS AND ANALYSIS

4.1. Sample characteristics

The sample used in this study was Ottawa sand (C-778), composed of nearly pure quartz. The elastic constants of the particles of solid were assumed as the average elastic constants of crystal quartz with $E_s = 86.85$ and $G_s = 31.14$ GPa.[‡] The corresponding Poisson's ratio, υ_s, is equal to 0.39. According to Procter and Barton [26], the frictional angle between quartz particles is 26°. Oda [27] found that the average co-ordination number, N, of a granular assembly had a strong correlation with void ratio, e, of the assembly, while was not affected by the grain size distribution. Chang *et al.* [28] collected published data [27,29,30] and suggested N can be estimated from void ratio using the following equation.

$$e = 1.66 - 0.125 \cdot N \tag{12}$$

The present work adopted the above empirical equation for the estimation of N.

[‡] data from http://www.crystran.co.uk/qutzdata.htm

4.2. Measured wave velocities

Specimens with two different relative densities, $D_r = 95\%$ ($e = 0.513$) and $D_r = 62.3\%$ ($e = 0.598$) were prepared and tested. The specimen with $D_r = 95\%$ represented a typical dense sand; and the specimen with $D_r = 62.3\%$ represented a typical medium dense sand for comparison. Figures 7 and 8, respectively, are the distributions of the *P*- and *S*-wave velocities along various directions of wave propagation for the specimen with $D_r = 95\%$. Figures 9 and 10, respectively, are the distributions of the *P*- and *S*-wave velocities along various directions of wave propagation for the specimen with $D_r = 62.3\%$. In these figures, 'L' denotes loading stage and 'U' denotes unloading stage. In Figures 7 and 9, the solid curves and the dotted curves, respectively, denote the distributions of *P*-wave velocities during the loading and unloading stages, respectively. In Figures 8 and 10, the solid curves and the dotted curves, respectively, denote the distributions of S_h- and S_v-wave velocities, respectively. In general, the wave velocities for $D_r = 95\%$ were relatively higher than the ones for $D_r = 62.3\%$.

Under a same vertical stress level, the velocity distribution in unloading stage appeared more isotropic than its counterpart in loading stage for $D_r = 62.3\%$. The difference in wave velocities during the loading and unloading stages corresponding to a same vertical stress implied a difference in contact stiffness distribution. Since fabric and stress state after unloading became relatively isotropic, the contact stiffness distribution became relatively isotropic as a result. The granular assembly of a loose or medium dense specimen after prepared by pluviation tended to contain more particle contacts along the vertical direction than along the horizontal direction. Initially, the concentration of contact normal along the vertical direction was likely more pronounced for the specimen with $D_r = 62.3\%$. The unloading stages in K_0 condition, however, resulted in a decrease of contact distribution density along the vertical direction as well as an increase along the horizontal direction. This tends to create a relatively isotropic distribution in fabric, and the horizontal stress became relatively close to the vertical stress. Hence, the wave velocity was relatively uniformly distributed.

On the contrary, the wave velocity distribution for dense specimen with $D_r = 95\%$ shows a different trend. It can also be explained by contact normal distribution. The dense specimen after prepared by pluviation, unlike looser specimen, would not contain significantly richer contact normal distributed along the vertical direction. Wave velocities appeared somewhat evenly distributed along various directions in the loading stages followed by pluviation. Wave velocity along an oblique direction with $\theta = 45^\circ$ was very close to that along the vertical direction in loading stages, as shown in Figure 7; it supports that the contact normal does not concentrate along the vertical direction.

The horizontally polarized body wave velocities were lower than the vertically polarized body wave velocities in the very beginning (when no vertical load except the gravity weights were applied). The result agrees with those by Yan and Byrne [31] and Agarwal and Ishibashi [32], but seems to contradictory to those by some others such as Knox *et al.* [33], Kopperman *et al.* [34], Chu *et al.* [35], Lee and Stokoe [36], Stokoe *et al.* [37], and Bellotti *et al.* [38]. Recently, Hoque and Tatsuoka [39] showed that the small strain stiffness of granular materials subjected to isotropic stress exhibited inherent anisotropy with $E_v > E_h$, where E_v and E_h denoted the vertical and the horizontal elastic Young's moduli. The initial stiffness anisotropy accounts for the reason of $V_{p\text{-}0} > V_{p\text{-}90}$ without applied vertical load (except the gravity weights). The terms $V_{p\text{-}0}$ and $V_{p\text{-}90}$, respectively, stand for the *P*-wave velocity along the vertical and the horizontal directions.

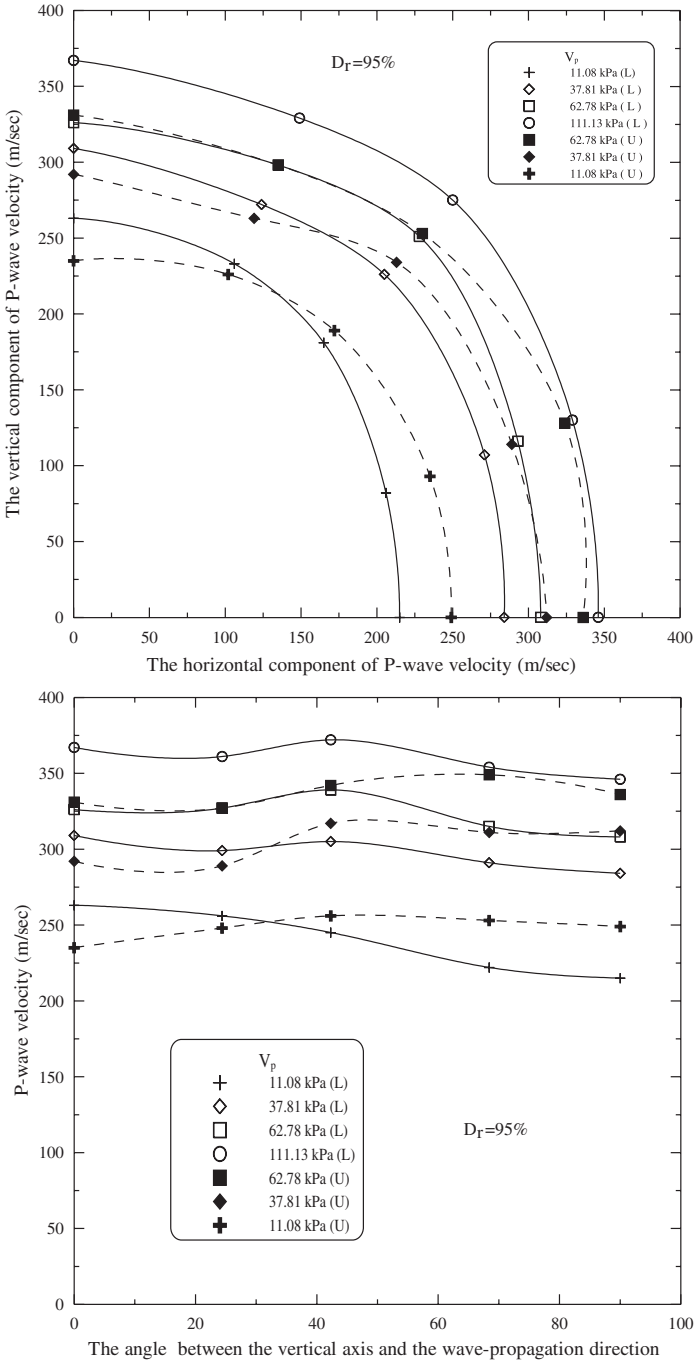

Figure 7. Distribution of *P*-wave velocities propagating along various directions in specimen with $D_r = 95\%$.

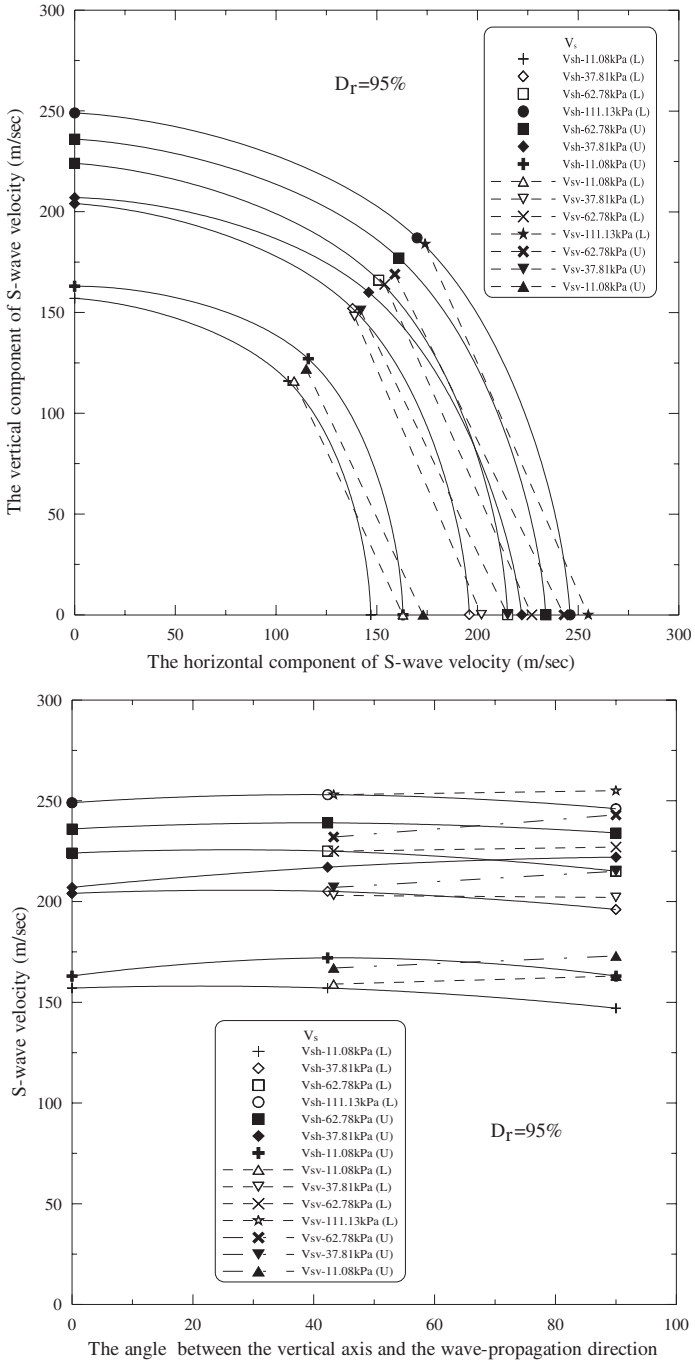

Figure 8. Distribution of *S*-wave velocities propagating along various directions in specimen with $D_r = 95\%$.

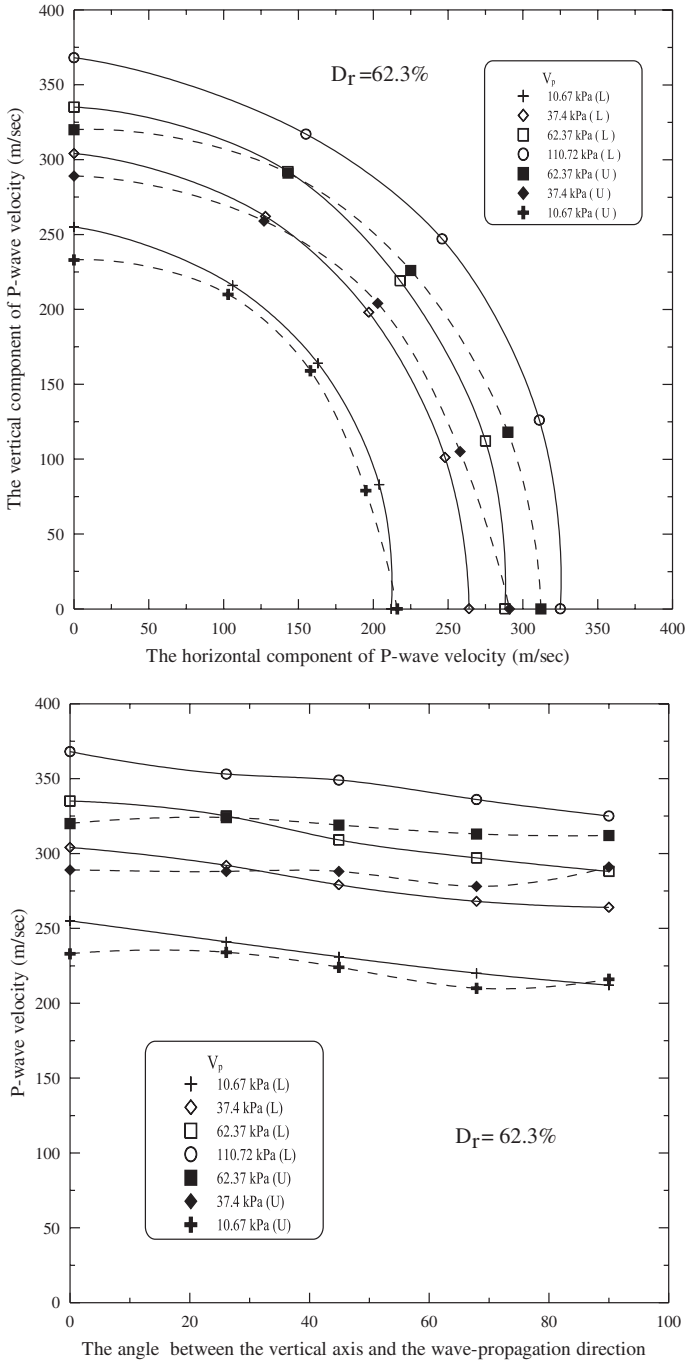

Figure 9. Distribution of *P*-wave velocities propagating along various directions in specimen with $D_r = 62.3\%$.

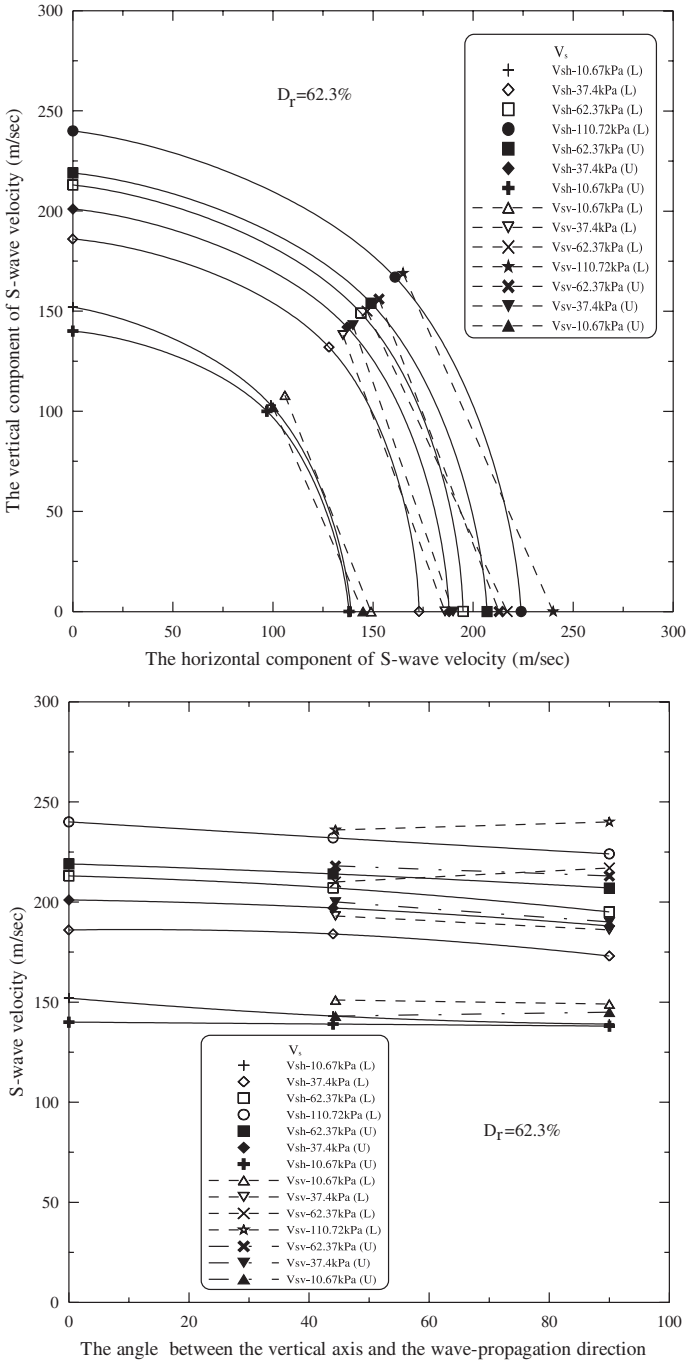

Figure 10. Distribution of *S*-wave velocities propagating along various directions in specimen with $D_r = 62.3\%$.

4.3. Measured stresses

A stack of eleven rings houses the tested specimen. Excluding rings near the top and bottom boundaries to reduce boundary effect, the stresses in intermediate rings close to the elevation of geophones were picked up for stress analysis. Tables II and III, respectively, list the lateral stresses measured at each ring and the average K_0 in various loading/unloading stages for the specimens of $D_r = 95$ and 62.3%, respectively. Figure 11 plots the average measured horizontal pressure against the applied vertical pressure in various loading/unloading stages.

The measured stresses show some interesting results. For the initially loading stages, K_0 for the specimen of $D_r = 95\%$ lies between 0.408 and 0.421 with an average of $K_0 = 0.413$, and K_0 for the specimen of $D_r = 62.3\%$ lies between 0.443 and 0.461, with an average of $K_0 = 0.451$. It confirms that K_0 for a specimen with a higher D_r appears to be lower than that of a specimen with lower D_r, which is supported by the well-known Jaky's empirical formula, $K_{0nc} = 1 - \sin\phi'$ [1]. An empirical correlation between the dry unit weight γ (in kPa). and the peak frictional angle (ϕ' in degrees) of air-pluviated Ottawa sand (C-778) was experimentally established by Chang [40] from the results of direct shear tests as follows (Figures 12 and 13):

$$\phi' = 6.43\gamma - 68.99 \tag{13}$$

Equation (13) is valid for $\gamma = 15.45$–$17.4\ \mathrm{kN/m^3}$ only. Using the above equation, the internal frictional angle corresponding to $D_r = 95\%$ (corresponding to $\gamma = 17.18\ \mathrm{kN/m^3}$) and $D_r = 62.3\%$ (corresponding to $\gamma = 16.26\ \mathrm{kN/m^3}$), respectively, were 41.5° and 35.6°. The K_0 estimated by the Jaky's equation corresponding to $\phi' = 41.5°$ and $\phi' = 35.6°$, respectively, were 0.337 and 0.418, respectively, comparing to the average measured values, 0.413 and 0.451.

K_0 of unloaded soil (K_{0u}) also depends on the overconsolidation ratio (OCR) and can be expressed in the following form [41]:

$$\frac{K_{0u}}{K_{0nc}} = \mathrm{OCR}^{\xi} \tag{14}$$

In the above equation, K_{0nc} is the K_0 value for the initially loaded soil, ξ is the at-rest rebound parameter. Mayne and Kulhawy [2] compiled available experimental data and

Table II. Lateral earth pressure measured at various rings and average K_0 ($D_r = 95\%$).

		Vertical stress (kPa)				
		Loading stages			Unloading stages	
	Ring No.	37.81	62.78	111.13	62.78	37.81
Horizontal stress (kPa)	4	12.9	21.7	41.6	33.3	23.5
	5	18.4	28.2	48.0	41.2	30.6
	6	18.5	28.5	48.2	41.2	30.2
	7	17.5	28.7	47.1	41.8	30.8
	8	12.3	21.7	41.8	33.9	23.7
Average horizontal stress (kPa)	4–8	15.92	25.76	45.34	38.28	27.76
Average K_0	4–8	0.421	0.410	0.408	0.610	0.734

Table III. Lateral earth pressure measured at various rings and average K_0 ($D_r = 62.3\%$).

		Vertical stress (kPa)				
		Loading stages			Unloading stages	
	Ring No.	37.4	62.37	110.72	62.37	37.4
Horizontal stress (kPa)	3	18.8	31.0	54.3	44.8	33.1
	4	15.0	26.3	49.0	39.6	27.9
	5	14.8	26.3	49.1	39.5	28.5
	6	17.7	28.9	52.0	42.6	31.1
	7	16.7	28.6	52.0	43.0	32.0
	8	17.3	28.6	51.5	42.2	30.4
	9	15.6	26.6	49.5	40.3	28.8
Average horizontal stress (kPa)	3–9	16.56	28.04	51.06	41.71	30.26
Average K_0	3–9	0.443	0.450	0.461	0.669	0.809

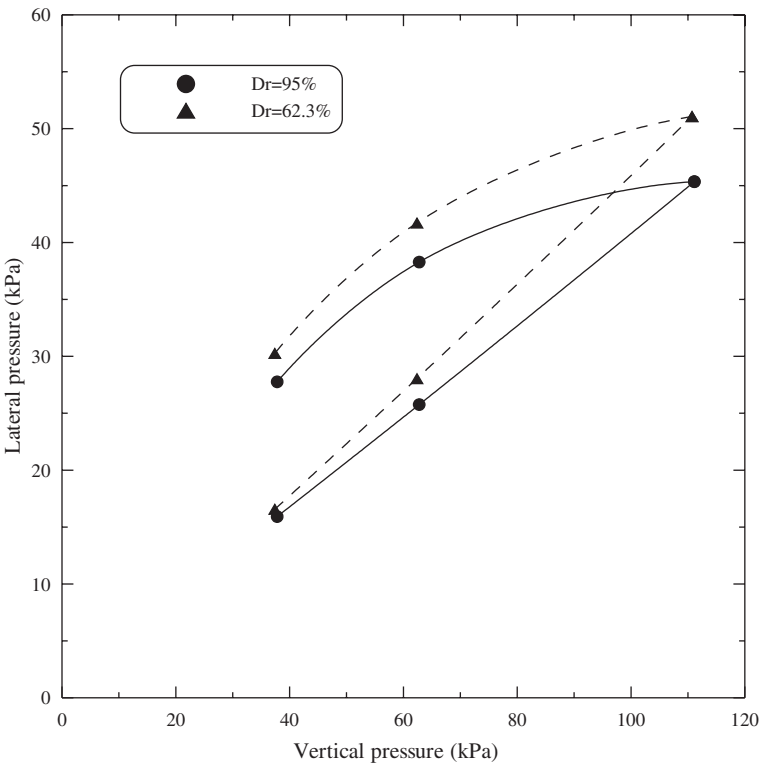

Figure 11. Measured lateral pressure against applied vertical pressure.

found ξ of sand was within 0.3 and 0.85. Table IV shows K_0 and the back calculated ξ for Ottawa sand. The data were from Edil and Dhowian [42] and the present experimental work. The at-rest rebound parameter ξ back calculated from the data of this work was

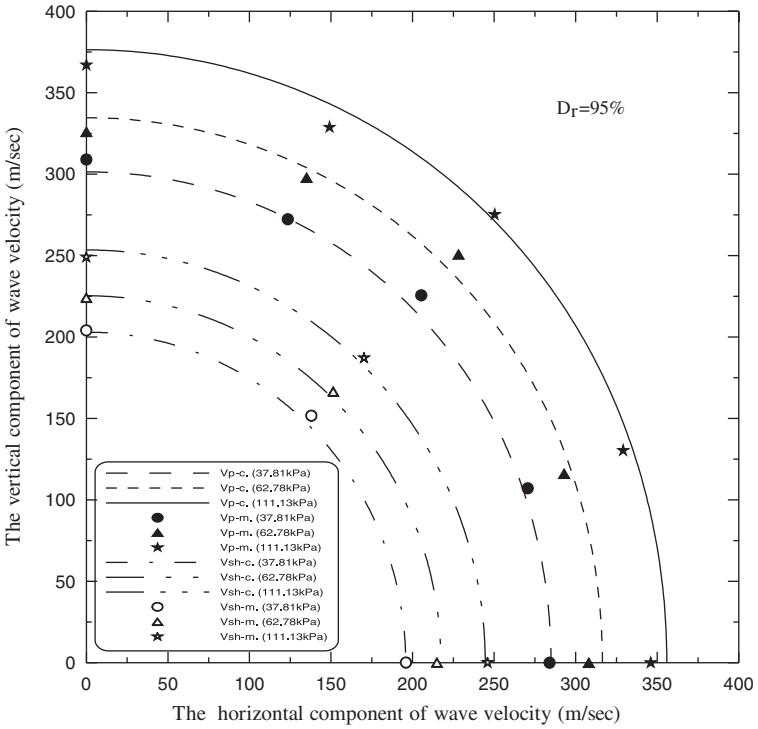

Figure 12. Comparison of the calculated and measured wave velocity distributions in loading stages for $D_r = 95\%$.

Table IV. Measured K_0 and back calculated.

	Void ratio	D_r in % (γ in kN/m^3)	Loading state	Stress level (kPa)	ϕ' in degrees	Direct measurement of K_0	Indirect determination of K_0 from $K_0 = 1 - \sin\phi'$	ξ
Ottawa sand	0.63	—	Loading	0–500	30.4	0.50	0.49	—
20-30 (Edil and	0.57	—	Loading	0–500	33.2	0.44	0.45	—
Dhowian, 1981)	0.54	—	Loading	0–500	34.6	0.41	0.43	—
Ottawa sand	0.598	62.3	Loading	0–110.72	35.6	0.451	0.418	—
C-778 (this		(16.265)	Unloading	62.37	—	0.669	—	0.571
research)			Unloading	37.4		0.809	—	
	0.513	95	Loading	0–111.13	41.5	0.413	0.337	—
		(17.181)	Unloading	62.78	—	0.610	—	0.566
			Unloading	37.81		0.734	—	

0.566 for $D_r = 95\%$ and 0.571 for $D_r = 62.3\%$, their values were quite close. The back calculated values of ξ for Ottawa sand (C-778) lie within the range reported by Mayne and Kulhawy [2].

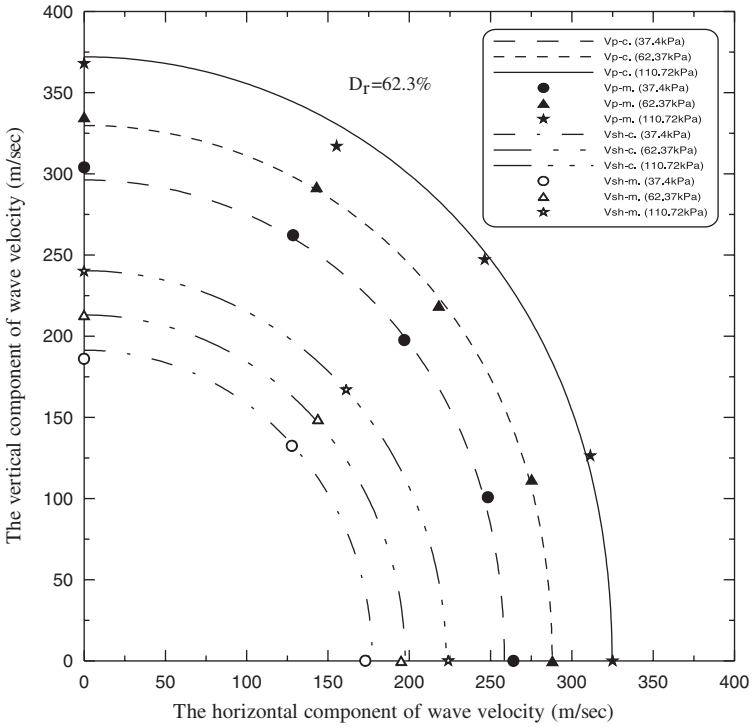

Figure 13. Comparison of the calculated and measured wave velocity distributions in loading stages for $D_r = 62.3\%$.

5. CALCULATED RESULTS AND DISCUSSION

5.1. Fabric parameter

The present work expressed fabric in the form of Equation (4). The specimen prepared by pluviation was assumed as a transversely isotropic material; in this condition, the directional distribution of fabric became axis-symmetrical. If the axis 3 is set parallel to the direction of pluviation, the plane 1–2 will become the plane of transverse isotropy. Consequently, fabric tensor will satisfy $D_{12} = D_{21} = D_{13} = D_{31} = D_{23} = D_{32} = 0$, and $D_{22} = D_{11} = -D_{33}/2$. Hence, merely one parameter D_{33} is required to describe fabric tensor for a pluviated specimen. A positive D_{33} means that more contact normal is along the direction of axis-3 than other directions. For a complete isotropic condition, all components of fabric tensor are zero; thus, $E(\mathbf{n}) = 1/4\pi$.

5.2. Calibrated results

In the present work, a specimen was maintained in K_0 condition and controlled vertical loads were applied to the specimen. Attempt was made to back calculate the horizontal stress from the measured wave velocities so that K_0 could be determined. In addition to K_0, the unknown during the calculation of stress state, however, also involved other unknown parameters. These

unknown parameters included the parameter D_{33} describing fabric, the parameter α characterizing the normal contact stiffness, and the parameter β characterizing the shear contact stiffness. The calibrated results (shown in Table V) were obtained through an optimization procedure by minimizing the object function defined by Equation (11).

In loading stages in K_0 condition, the changes in geometric fabric were small. To allow more data for the back-calculation, geometric fabrics were assumed unchanged during the whole loading process. The geometric fabric calculated in this manner was regarded as an average in the loading stages. For each specimen, a total of thirty wave velocities (10 each from the applied loading steps of 26.73, 51.7, 100.05 kPa) measured from three initially loaded stages were used to calibrate K_0 in the initially loaded states. With sufficient data (i.e. 30 wave-velocities) for calibration, the converged results clearly identified the global minimum. Figures 12 and 13, respectively, compare the calculated and measured wave velocity distributions in loading stages for $D_r = 95$ and 62.3%, respectively. The averages of normalized differences between a set of n calculated wave velocities V_c and measured wave velocities V_m, defined as $\sqrt{\sum_{i=1}^{n}((V_m - V_c)/V_c)_i^2/n}$, were 1.8 and 1.4%, respectively, for $D_r = 95$ and 62.3%. The calculated wave velocities were obtained with the calibrated parameters shown in Table V. In the legends of these figures, $V_{p\text{-}c}$ denotes the calculated P-wave velocity, $V_{p\text{-}m}$ denotes the measured P-wave velocity, $V_{sh\text{-}c}$ denotes the calculated S_h-wave velocity, and $V_{sh\text{-}m}$ denotes the measured S_h-wave velocity. The calculated wave velocities distributions agree well with the measured distribution.

For unloaded specimen, K_0 varies with vertical stress. Hence, calibration had to be carried out individually for each vertical stress. Due to the fact that less wave velocities (only ten) were used to calibrate K_0 for each unloading case, higher possible error from calibration is expected. Figures 14 and 15, respectively, compare the calculated and measured wave velocity distributions in unloading stages for $D_r = 95$ and 62.3%, respectively. The averages of normalized differences between the calculated and measured wave velocities in the unloading stages were 2.0 and 1.6%, respectively, for $D_r = 95$ and 62.3%. The global minimum is improvable if more wave-velocity measurements could be made along various directions of wave-propagation. It is noted that a higher order form of fabric tensor may also be introduced in order to improve the capability for describing directional distribution of geometric fabric.

Table V presents the calibrated results for various conditions. Discussion on these results follows.

Table V. Results of calibration.

		σ_v (kPa)	Measured parameter	Calibrated parameters			
			K_0	α	β	D_{33}	K_0
$D_r = 95\%$	Loading stages	37.81–111.13	0.408–0.421	0.295	0	−0.087	0.411
	Unloading stages	62.78	0.610	0.295	0	−0.258	0.679
		37.81	0.734	0.295	0.02	−0.419	0.735
$D_r = 62.3\%$	Loading stages	37.4–110.72	0.443–0.461	0.292	0.08	0.244	0.465
	Unloading stages	62.37	0.669	0.292	0.35	0.033	0.665
		37.4	0.809	0.290	0.07	0.052	0.865

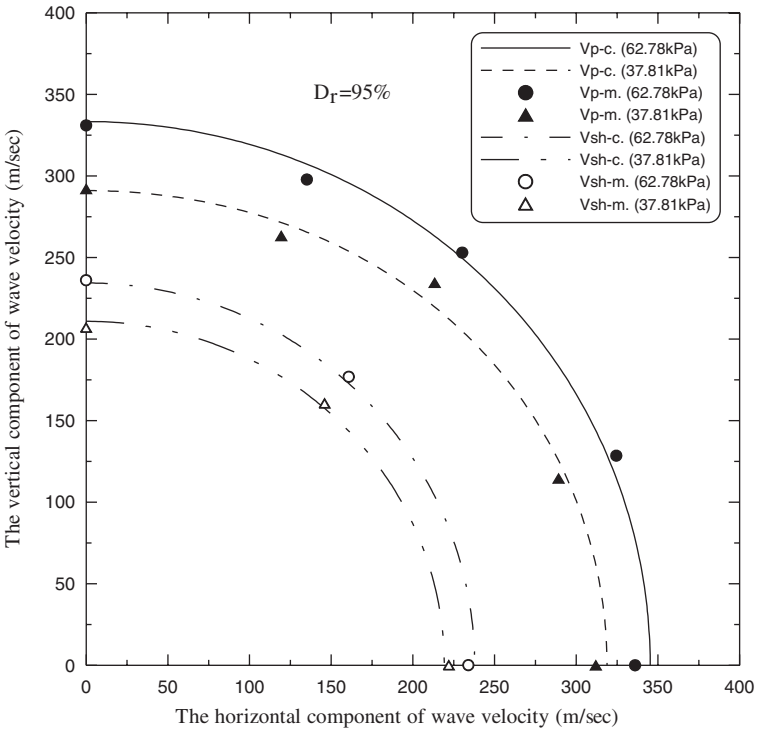

Figure 14. Comparison of the calculated and measured wave velocity distributions in unloading stages for $D_r = 95\%$.

(1) Normal contact stiffness parameter α

The normal contact stiffness can be expressed in the form of $k_n = C_1 \cdot f_n^{\gamma} = C_1 \cdot f_n^{1-2\alpha}$. The parameter α implicitly reveals the dependence of normal contact stiffness on normal contact force. According to the Hertz contact theory, γ is equal to 1/3 (i.e. $\alpha = 1/3$); but based on the assumption of cone-to-plane contact [43], γ should equal to 1/2 (i.e. $\alpha = 1/4$). Considering that the contact mechanism of sand particles may be inelastic, nonlinear, rough contact, and non-circular, Chang *et al.* [44] pointed out that γ and C_1, respectively, for sand particles may be somewhat higher and lower than what Hertz–Mindlin theory predicts [45]. Experimental data [46] supports γ actually lies between 1/3 and 1/2. Hence, for the calibration of α the upper and lower limits, respectively, were set to 1/3 and 1/4. All calibrated values of α were between the upper and the lower limits.

(2) Shear contact stiffness parameter β

The parameter β implicitly reveals the dependence of shear contact stiffness on the level of shear contact force. Mindlin and Deresiewicz [47] studied the shear contact compliance between two elastically contacted spheres under varying oblique forces. For a particulate assembly, however, every particle may contact with several other particles. It seems unlikely that all shear contact stiffness of particles can satisfy the shear contact conditions assumed by Mindlin and Deresiewicz [47]. Furthermore, it may be difficult to employ the incremental form of shear contact relations practically. For these concerns, the present work expressed the shear contact

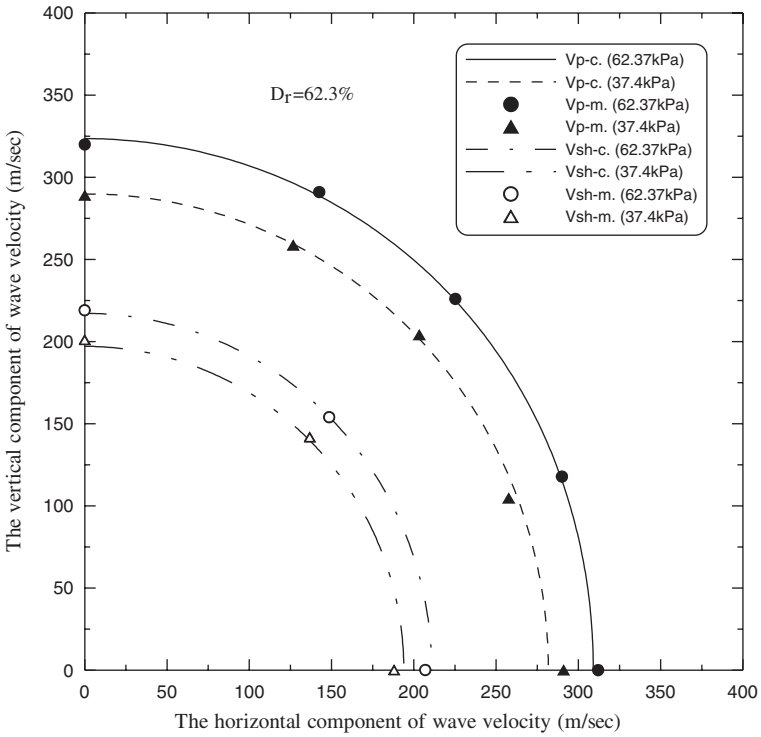

Figure 15. Comparison of the calculated and measured wave velocity distributions in unloading stages for $D_r = 62.3\%$.

stiffness in the following form.

$$k_r = C_2 \cdot \left(1 - \frac{f_r}{f_n \cdot \tan \phi_\mu}\right)^{\beta} \cdot k_n \quad \text{as } f_r < f_n \cdot \tan \phi_\mu \tag{15}$$

$$k_r = 0 \quad \text{for } f_r \geqq f_n \cdot \tan \phi_\mu \tag{16}$$

During the calibration of K_0, the parameter β was also treated as an unknown. A non-negative constraint was set for β. The minimum condition $\beta = 0$ implies that there is no local slippage takes place at the contact-point and the shear contact stiffness does not depend on the shear contact-force. The calibrated values of β for $D_r = 62.3\%$ were generally larger than those for $D_r = 95\%$ which were near 0. It makes sense because that the average co-ordination number for $D_r = 62.3\%$ should be less than that for $D_r = 95\%$, while a particle assembly with larger average co-ordination number would be subjected to a stronger constraint.

(3) Fabric Parameter

The calibrated values of D_{33} for different D_r reveal interesting information. The fabric parameter D_{33} in loading stages for very dense Ottawa sand ($D_r = 95\%$) was in general close to 0, which suggests that the contact normal distribution of the granular assembly at a very dense state tends to be more isotropic or directionally uniform. The fabric parameter D_{33}, however,

became negative in unloading stages; it implies that the number of contacts turned to be more abundant along the horizontal direction than along the vertical direction. On the other hand, D_{33} of medium dense Ottawa sand ($D_r = 62.3\%$) in the initially loading stages was 0.244, which implied the number of contact points was significantly more abundant along the vertical direction than along the horizontal direction. Unloading in K_0 condition results in a decrease of the contact distribution density along the vertical direction and an increase along the horizontal direction. As a result, D_{33} of the unloaded sand ($D_r = 62.3\%$) decreased and approached to 0, which showed that the fabric of the medium dense sand became more isotropic after unloading.
(4) Stress coefficient K_0

The calibrated value of K_0 for the very dense sand ($D_r = 95\%$) in the initially loading stages was 0.411. This calibrated K_0 agreed with the measured K_0 (0.408–0.421, with an average of $K_0 = 0.413$) very well. For unloading stages, the calibrated K_0 for $\sigma_v = 62.78$ and 37.81 kPa, respectively, were 0.679 and 0.735. Compared with the measured K_0 (0.61 and 0.734, respectively, for $\sigma_v = 62.78$ and 37.81 kPa) in unloading stages, the errors were 11 and 0.1%, respectively, for $\sigma_v = 62.78$ and 37.81 kPa. The calibrated value of K_0 for the medium dense sand ($D_r = 62.3\%$) in the initially loading stages was 0.465. This calibrated K_0 also agreed with the measured K_0 (0.443–0.461, with an average of $K_0 = 0.451$) acceptably, with an error of 3%. For unloading stages, the calibrated K_0 for $\sigma_v = 62.37$ and 37.4 kPa, respectively, were 0.665 and 0.865. Compared with the measured K_0 (0.669 and 0.809, respectively, for $\sigma_v = 62.37$ and 37.4 kPa) in unloading stages, the errors were 0.6 and 7%, respectively.

Due to the fact that less wave velocities were available for calibrating K_0 in each unloading stage, larger differences between the back calculated and the measured K_0 could be expected. However, it should be noted that the K_0 prediction could be improved if more measurement of wave velocities along more directions of wave propagation could be made.

6. SUMMARY AND CONCLUSIONS

This study aims to explore the possibility for the determination of the *in situ* lateral stress in level-ground of granular soil by seismic methods on the basis of micromechanics theory. The present work made use of a field simulator to model the *in situ* stress condition. This field simulator can control a K_0 condition in large specimens (diameter = 784 mm) prepared by air-pluviation. A series of vertical loading containing subsequent loading and unloading were applied to the specimen. The lateral stress were measured and compared with the empirical formula for predicting K_0. In general, the K_0 values determined experimentally in this work is in accordance with the exiting empirical relations.

Several geophones were installed in large specimens (diameter = 784 mm); the wave velocities along various directions were measured. The idea was to simulate the *in situ* cross-hole seismic method for the measurement of wave velocities along various directions of wave propagation in a level ground. Knowing the vertical stress of the specimen, the lateral stress was calibrated from the series of wave-velocities. The methodology for determining the lateral stress employed the theories of micromechanics and anisotropic wave propagation. The value of K_0 was calibrated using an optimization procedure combined with the genetic algorithm and nonlinear optimization. This methodology is valid for a transversely isotropic granular assembly.

For loading stages in K_0 condition, back-calculated result suggests that the contact normal of very dense Ottawa sand distributed rather evenly along various directions. Medium dense

Ottawa sand, on the other hand, appeared to have a more anisotropic distribution of contact, with more contact along the vertical direction than along the lateral direction. The consistency of the back-calculated and measured K_0 demonstrated the feasibility for the determination of the *in situ* lateral stress in level-ground of granular soil by seismic methods on the basis of micromechanics theory as long as enough data of wave-velocity measurements along various directions of wave-propagation were available.

With the *in situ* cross-hole seismic method, it will not be difficult to obtain wave-velocities along as many different directions of wave-propagation as possible. Consequently, the usage of the presented methodology for determining K_0 in level ground of granular soil by seismic methods seems encouraging.

ACKNOWLEDGEMENTS

The National Science Council of the Republic of China under Contract No. NSC90-2211-E-009-068 financially supported this work. This support is gratefully acknowledged.

REFERENCES

1. Jaky J. The coefficient of earth pressure at rest. *Journal for Society of Hungarian Architects and Engineers* 1944; 355–358.
2. Mayne PW, Kulhawy FH. K_0-OCR relationships in soil. *Journal of the Geotechnical Engineering Division* (ASCE) 1982; **108**(GT6):851–872.
3. Massarsch KR. New method of measurement of lateral earth pressure in cohesive soils. *Canadian Geotechnical Journal* 1975; **12**(1):142–146.
4. Marchetti S. A new in situ test for the measurement of horizontal soil deformability. *Proceeding of the American Society of Civil Engineers Speciality Conference In situ Measurement of Soil Properties*, *Raleigh*, vol. 2, 1975; 255–269.
5. Menard L. An apparatus for measuring the strength of soils in place. *M.Sc. Thesis*, University of Illinois, Urbana, IL, 1956.
6. Baguelin F, Jezequel JF, Le Mee E, Le Melhaute A. Expansion of cylindrical probes in cohesive soils. *Journal of the Soil Mechanics and Foundations Division*, ASCE, 1972; **98**(SM11):1129–1142.
7. Wroth CP, Hughes JMO. An instrument for the *in situ* measurement of the properties of soft clays. *Proceedings of the 8th International Conference on Soil Mechanics and Foundation Engineering*, Moscow 1973; 487–494.
8. Campanella RG, Robertson PK. A seismic cone penetrometer to measure engineering properties of soil. *Proceedings of the 54th Annual Mtg Society Exploration Geophysics*, Atlanta 1984.
9. Baldi G, Bruzzi D, Superbo S, Battaglio M, Jamiolkowski M. Seismic cone in Po River sand. *Proceedings of International Symposium on Penetration Testing*, *ISOPT-1*, Orlando, Balkema, 1988; 643–650.
10. Sully JP, Campanella RG. In situ shear wave velocity determination using seismic cone penetrometer for evaluating soil anisotropy. *Proceedings of the 10th World Conference on Earthquake Engineering*, Madrid, 1992; 1269–1274.
11. Nishio S, Katsura Y. Shear wave anisotropy in Edogawa Pleistocene deposit. *Proceedings of the International Symposium on Pre-failure Deformation Characteristics of Geomaterials*, Sapporo, 1994; 169–174.
12. Roesler S. Anisotropic shear modulus due to stress anisotropy. *Journal of the Geotechnical Engineering Division* (ASCE) 1979; **105**(GT7):871–880.
13. Sully JP, Campanella RG. Evaluation of in situ anisotropy from crosshole and downhole shear wave velocity measurements. *Geotechnique* 1995; **45**(2):267–282.
14. Fioravante V, Jamiolkowski M, Lo Presti DCF, Manfredini G, Pedroni S. Assessment of the coefficient of the earth pressure at rest from shear wave velocity measurements. *Geotechnique* 1995; **48**(5):657–666.
15. Pan YW, Dong JJ. A micromechanics-based methodology for evaluating the fabric of granular material. *Geotechnique* 1999; **49**(6):761–775.
16. Chang CS, Misra A. Packing structure and mechanical properties of granulates. *Journal of Engineering Mechanics* 1990; **116**(5):1077–1093.
17. Kanatani K. Distribution of directional data and fabric tensors. *International Journal of Engineering Science* 1984; **22**(2):149–164.

18. Rothenburg L. Micromechanics of idealized granular systems. *Ph.D. Thesis*, Carleton University, Ottawa, 1980.
19. Liou JC, Pan YW. Fabric evolution of granular assembly under K_0 loading/unloading. *International Journal for Numerical and Analytical Methods in Geomechanics* 2003; **27**(13):1099–1122.
20. Chang CS, Chao SJ, Chang Y. Estimates of elastic moduli for granular material with anisotropic random packing structure. *International Journal of Solids and Structures* 1995; **32**(14):1989–2008.
21. White JE. *Seismic Waves*: *Radiation*, *Transmission*, *and Attenuation*. McGraw-Hill: 1965.
22. Goldberg DE. *Genetic Algorithm in Search*, *Optimization and Machine Learning*. Addison-Wesley Publishing Company: MA, 1989.
23. Marquardt D. An algorithm for least-squares estimation of nonlinear parameters. *SIAM Journal on Applied Mathematics* 1963; **11**:431–441.
24. Hsu HH, Huang AB. Development of an axisymmetric field simulator for cone penetration tests in sand. *Geotechnical Testing Journal* 1998; **21**(4):348–355.
25. Stokoe KH, II, Mok YS, Lee N, Lopez R. In situ seismic methods: recent advances in testing, understanding and applications. *Proceedings of the 14th Conference Geotechniques*, Turin 1989.
26. Procter DC, Barton RR. Measurements of the angle of interparticle friction. *Geotechnique* 1974; **24**(4):581–604.
27. Oda M. Co-ordination number and its relation to shear strength of granular material. *Soils and Foundations* 1977; **17**(2):29–42.
28. Chang CS, Misra A, Sundaram SS. Properties of granular packings under low amplitude cyclic loading. *Soil Dynamics and Earthquake Engineering* 1991; **10**(4):201–211.
29. Marsal RJ. Mechanical properties of rockfill. *Embankment Dam Engineering* 1973; 109–145.
30. Yanagisawa E. Influence of void ratio and stress condition on the dynamic shear modulus of granular media. *Advances in the Mechanics and the Flow of Granular Materials* 1983; 947–960.
31. Yan L, Byrne P. Simulation of downhole and crosshole seismic tests on sand using the hydraulic gradient similitude method. *Canadian Geotechniques Journal* 1990; **27**:441–460.
32. Agarwal TK, Ishibashi I. Anisotropic elastic constants of granular assembly from wave velocity measurements. In *Advances in Micromechanics of Granular Materials*. Elsevier: Amsterdam, 1992.
33. Knox DP, Stokoe II KH, Kopperman SE. Effect of state of stress on velocity of low amplitude shear waves propagating along principal stress directions in dry sand. *Report GR 82-23*. University of Texas at Austin 1982.
34. Kopperman SE, Stokoe II KH, Knox DP. Effect of state of stress on velocity of low amplitude compression waves propagating along principal stress directions in dry sand. *Report GR 82-22*. University of Texas at Austin 1982.
35. Chu HYF, Lee SHH, Stokoe II KH. Effects of structural and stress anisotropy on velocity of low amplitude compression waves propagating along principal stress directions in dry sand. *Report GR 84-6*. University of Texas at Austin 1984.
36. Lee SHH, Stokoe II KH. Investigation of low amplitude shear wave velocity in anisotropic material. *Report GR 86-6*, University of Texas at Austin 1986.
37. Stokoe II KH, Lee JNK, Lee SHH. Characterization of soil in calibration chamber with seismic waves. *Proceedings of ISOCCT1*, Potsdam, NY, 1991.
38. Bellotti R, Jamiolkowski M, Lo Presti DCF, O'Neill DA. Anisotropy of small strain stiffness in Ticino sand. *Geotechnique* 1996; **46**(1):115–131.
39. Hoque E, Tatsuoka F. Anisotropy in elastic deformation of granular materials. *Soils and Foundations* 1998; **38**(1):163–179.
40. Chang SY. Effects of backfill density on active earth pressure. *Master Thesis*, Dept. of Civil Engineering, National Chiao Tung University, Hsinchu, Taiwan, R.O.C., 2000.
41. Schmidt B. Discussion of 'Earth pressures at rest related to stress history'. *Canadian Geotechnical Journal* 1966; **3**(4):239–242.
42. Edil TB, Dhowian AW. At-Rest lateral pressure of peat soils. *Journal of the Geotechnical Engineering Division* (ASCE) 1981; **107**(GT2):201–217.
43. Goddard JD. Nonlinear elasticity and pressure-dependent wave speeds in granular media. *Proceedings of the Royal Society of London, London, Series A*, 1990; **430**:105–131.
44. Chang CS, Sundaram SS, Misra A. Initial moduli of particulate mass with frictional contacts. *International Journal for Numerical and Analytical Methods in Geomechanics* 1989; **13**(6):629–644.
45. Johnson KL. *Contact Mechanics*. Cambridge University Press: London, 1985.
46. Hardin BO, Richart FE. Elastic wave velocities in granular soils. *Journal of Soil Mechanics Foundation Division* Proceedings (ASCE) 1963; **89**(SM1):33–65.
47. Mindlin RD, Deresiewicz H. Elastic spheres in contact under varying oblique forces. *Journal of Applied Mechanics* (ASME) 1953; **20**(3):327–344.

